nature materials

LETTERS

PUBLISHED ONLINE: 25 MAY 2014 | DOI: 10.1038/NMAT3990

A stable three-dimensional topological Dirac semimetal Cd_3As_2

Z. K. Liu[1†], J. Jiang[2,3†], B. Zhou[2,4†], Z. J. Wang[5†], Y. Zhang[1,4], H. M. Weng[5], D. Prabhakaran[2], S-K. Mo[4], H. Peng[2], P. Dudin[6], T. Kim[6], M. Hoesch[6], Z. Fang[5], X. Dai[5], Z. X. Shen[1], D. L. Feng[3], Z. Hussain[4] and Y. L. Chen[1,2,4,6★]

Three-dimensional (3D) topological Dirac semimetals (TDSs) are a recently proposed state of quantum matter[1–6] that have attracted increasing attention in physics and materials science. A 3D TDS is not only a bulk analogue of graphene; it also exhibits non-trivial topology in its electronic structure that shares similarities with topological insulators. Moreover, a TDS can potentially be driven into other exotic phases (such as Weyl semimetals[1,7], axion insulators[1,4] and topological superconductors[8,9]), making it a unique parent compound for the study of these states and the phase transitions between them. Here, by performing angle-resolved photoemission spectroscopy, we directly observe a pair of 3D Dirac fermions in Cd_3As_2, proving that it is a model 3D TDS. Compared with other 3D TDSs, for example, β-cristobalite BiO_2 (ref. 3) and Na_3Bi (refs 4,5), Cd_3As_2 is stable and has much higher Fermi velocities. Furthermore, by *in situ* doping we have been able to tune its Fermi energy, making it a flexible platform for exploring exotic physical phenomena.

The study of the electronic structure of solids is one of the central tasks in materials science. Conventionally, band theory classifies materials into insulators and metals depending on whether there exists a finite bandgap. Recently, it was realized that the insulators can be further classified into normal and topological insulators according to the topology of their electronic structures[8,10].

Interestingly, in the transition from insulators to metals, there exists an intermediate state, in which the conduction and valence band touch only at discrete points, leading to a zero bandgap and singular points at the Fermi surface—and graphene is a well-known example. Remarkably, although this state was already proposed at the early age of the band theory[11], its topological classification was recognized only recently[1–4,6,12,13]: in analogy to topological insulators, the non-trivial topology of the band structure in semimetal also leads to a new state of matter, TDSs[1–6].

Unlike the 2D Dirac fermions in graphene or on the surface of 3D topological insulators[8,10,14,15], a 3D TDS possesses bulk Dirac fermions that disperse linearly along all three momentum directions. This unique electronic structure makes the 3D TDS not only a host of many unusual phenomena (for example, unusually high bulk carrier mobility[16], high-temperature linear quantum magnetoresistance[17,18], oscillating quantum spin Hall effect[4,19] and giant diamagnetism[20,21]), but also a possible platform to realize various applications of graphene in 3D materials. In addition, unlike graphene[22], the 3D Dirac fermions in a TDS are robust against the spin–orbit interaction[4,6].

Besides these unusual properties, a TDS can also be driven into many other quantum states, such as the Weyl semimetal[1,7], axion insulator[1,4] and topological superconductor[8,9], when additional symmetry is broken. This versatility makes the TDS an ideal platform for the realization of other materials and the study of various topological quantum phase transitions.

Here, we use angle-resolved photoemission spectroscopy (ARPES) to investigate the electronic structure of a 3D TDS candidate, Cd_3As_2 (ref. 6). By mapping out the band dispersions along the k_x, k_y and k_z momentum directions, we discovered that Cd_3As_2 possesses a pair of 3D Dirac fermions near the Γ point with strong anisotropy between the k_z and k_x/k_y directions. Furthermore, by using *in situ* alkaline metal doping, we successfully tuned the position of the Fermi energy (E_F) into the conduction band, which not only enables us to observe the upper half (unoccupied) Dirac cone, but also makes it a more practical material for future functional device applications, especially with its unusually high carrier mobility[16].

A crystallographic cell of Cd_3As_2 is shown in Fig. 1a, which comprises an intercalated face-centred cubic (fcc) arsenic sublattice and a cubic cadmium sublattice with two vacancies[23]. For ARPES measurements, we cleaved Cd_3As_2 single crystals *in situ* in the ultrahigh-vacuum measurement chamber, and the natural cleavage plane is along the [111] direction of the fcc As sublattice (Fig. 1a,b). The corresponding 3D Brillouin zone and its projection on the k_x–k_y plane perpendicular to the [111] direction are illustrated in Fig. 1c,d, respectively, with high-symmetry points indicated.

The core-level photoemission spectrum of Cd_3As_2 is shown in Fig. 1e, from which the characteristic doublet peaks of Cd and As elements are clearly observed. The Laue pattern (Fig. 1e inset) and the broad Fermi surface mapping covering more than 10 Brillouin zones (Fig. 1f) both demonstrate the (111) cleaved surface; and the Brillouin zone size obtained in Fig. 1f agrees well with the lattice constant indicated in Fig. 1b.

To illustrate the overall band structure of Cd_3As_2, the photoemission spectrum covering a large energy scale along the $\overline{M}$–$\overline{\Gamma}$–$\overline{M}$ direction is shown in Fig. 2a (where mixed photon polarization is used to see multiple bands). As bulk bands with different orbital characters have different photoemission cross-sections for given photon polarization and measurement geometry

[1]Stanford Institute for Materials and Energy Sciences, SLAC National Accelerator Laboratory, 2575 Sand Hill Road, Menlo Park, California 94025, USA, [2]Physics Department, Clarendon Laboratory, University of Oxford, Parks Road, Oxford OX1 3PU, UK, [3]State Key Laboratory of Surface Physics, Department of Physics, and Advanced Materials Laboratory, Fudan University, Shanghai 200433, China, [4]Advanced Light Source, Lawrence Berkeley National Laboratory, Berkeley, California 94720, USA, [5]Beijing National Laboratory for Condensed Matter Physics and Institute of Physics, Chinese Academy of Sciences, Beijing 100190, China, [6]Diamond Light Source, Didcot OX11 0DE, UK. †These authors contributed equally to this work.
*e-mail: Yulin.Chen@physics.ox.ac.uk

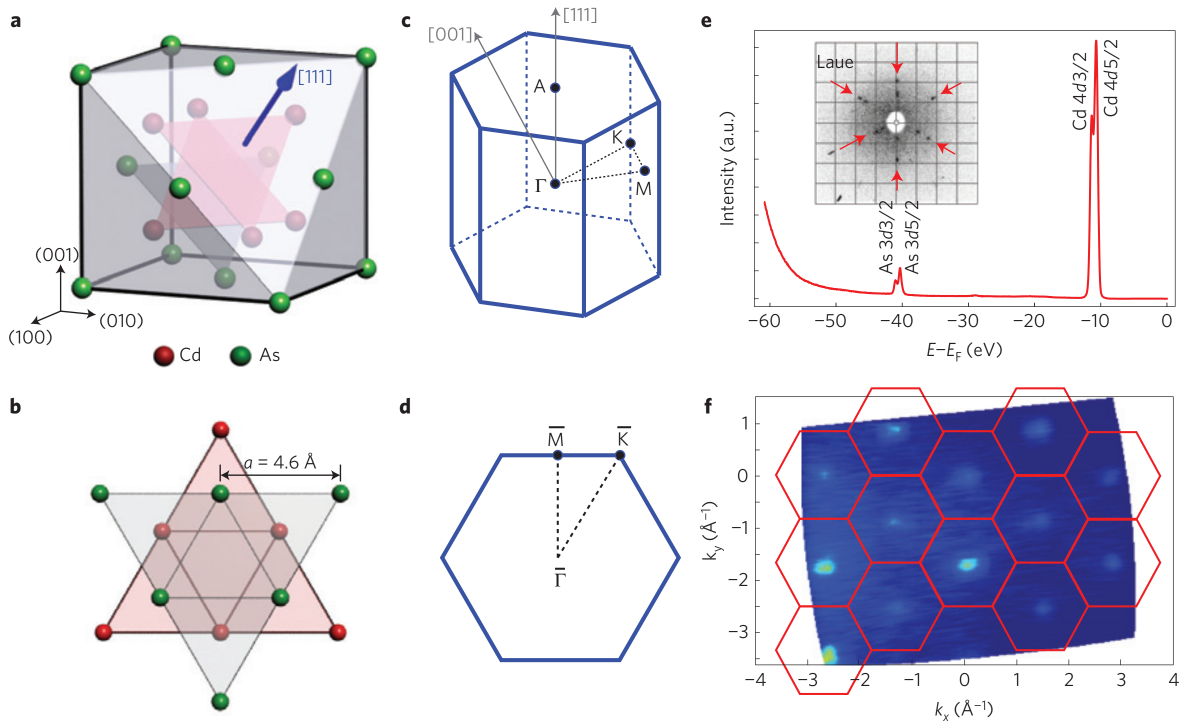

Figure 1 | Crystal structure of Cd_3As_2 and Fermi surface measured by ARPES. a, Crystal structure of Cd_3As_2, showing an intercalated Cd cubic lattice (with two vacancies) inside the fcc As lattice. The blue arrow indicates the normal of the (111) surface, where the crystal naturally cleaves. **b**, Projected view of the lattice along the [111] direction, showing the stacking As and Cd layers with in-plane lattice constant $a = 4.6$ Å. **c**, Bulk Brillouin zone of Cd_3As_2 (111) with high-symmetry points indicated. Grey arrows indicate the [001] and [111] directions, respectively. **d**, Projected surface Brillouin zone in the k_x–k_y plane. **e**, Core-level photoemission spectrum clearly shows the characteristic Cd 4*d* and As 3*d* doublets. Inset is the Laue pattern of the sample used in ARPES measurements (indicated by the red arrows), confirming that the cleaved plane is along the [111] direction. **f**, Broad Fermi surface map covering 13 Brillouin zones, again confirming the (111) cleave plane and the lattice constant in **b**, and the overlaid red hexagons indicate the Brillouin zones. The uneven intensity of the Fermi surface at different Brillouin zones results from the matrix element effect.

due to matrix element effects[24,25], we were able to select proper photon polarization to study the 3D Dirac fermions and minimize the influence of other bulk bands. As can be seen in Fig. 2b, the intensity of the Dirac band is enhanced when the photon polarization is in parallel with the $\bar{M}$–$\bar{\Gamma}$–$\bar{M}$ direction (schematic of the measurement can be found in Supplementary Information, part A). Thus, in the rest of this letter, we use the measurement geometry in Fig. 2b for the study of the 3D Dirac fermions in Cd_3As_2.

Owing to its 3D nature, to locate the Dirac points, we need to measure the electronic structure not only along the k_x and k_y directions (as in Fig. 1f), but also along the k_z direction—which can be achieved by performing photon-energy-dependent ARPES measurements[24,25] (the principle, details and the determination of the k_z locations can be found in Supplementary Information, part B).

By performing the measurements under a broad range of photon energies (60–225 eV) to determine the exact k_z position (see Supplementary Information, part B for details), we obtained the Fermi surface map of Cd_3As_2 throughout the entire 3D Brillouin zone (Fig. 2c), which clearly shows a pair of point-like Fermi surfaces in the vicinity of Γ originating from the 3D Dirac points, with $k_z = \pm 0.16$ Å^{-1} along the [111] direction. By using the crystal structure in Fig. 1a, our *ab initio* calculation (see Supplementary Information part D for details) suggests the Dirac points' positions at $k_z = \pm 0.12$ Å^{-1}, which is close to our measurements. To investigate the k_z dispersion of the 3D Dirac cone, in Fig. 2d we show four band dispersions measured at different k_z locations, from the *A* point (panel (i)) to the Dirac point (panel (iv)). Clearly, the dispersions evolved from a hyperbolic (Fig. 2d(i–iii), more details of the fitting can be found in Supplementary Information, part C) to a linear shape (Fig. 2d(iv)), showing the typical characteristic of a Dirac cone—which will be further discussed below.

With the complete mapping of the 3D Brillouin zone, we were able to locate the Dirac points and study the dispersions along all three (k_x, k_y and k_z) momentum directions. In Fig. 3b, the cone-shape dispersion along the k_x and k_y directions is demonstrated, in which the 3D plot of the ARPES spectra intensity clearly shows linear dispersions along both directions with little anisotropy (the Fermi velocity determined as $V_x = 8.47$ eV Å or 1.28×10^6 m s^{-1} and $V_y = 8.56$ eV Å or 1.3×10^6 m s^{-1}, respectively). In Fig. 3c, the contour plots at different binding energies also show a cone-shape dispersion that evolves from a point (the Dirac point) to a ring shape at higher binding energies.

To prove the 3D nature of the Dirac cone, we need to investigate the band dispersion along the k_z direction as well, which was achieved by performing photon-energy dependent ARPES measurements as discussed above (more details can be found in Supplementary Information, part B). As shown in Fig. 3d, for a 3D Dirac fermion, ARPES measurements at different k_z locations should also yield either linear or hyperbolic dispersions depending on whether the ARPES measurement cuts through the Dirac point. Obviously, both kinds of dispersion are different from the usual parabolic shape typically seen from massive electron systems.

In Fig. 3e, we show five ARPES measurements from different k_z locations to illustrate the typical dispersions (as shown in Fig. 3d) that can be well fitted by either linear or hyperbolic curves. Similar to Fig. 3b, we plot the 3D ARPES spectra in Fig. 3f, which clearly show an elongated Dirac cone (along the k_z direction, see Fig. 3d) with a much smaller velocity along the k_z direction: $V_z = 2.16$ eV Å or 3.27×10^5 m s^{-1}. Compared

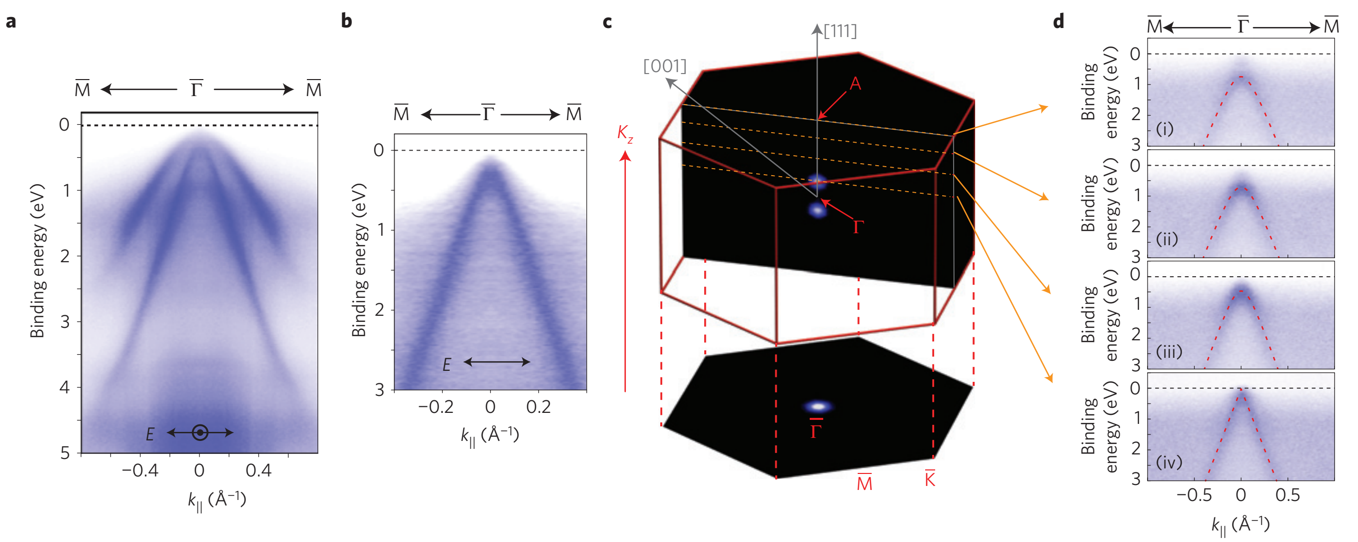

Figure 2 | General electronic structure of Cd_3As_2 with strong k_z dependence. a, Band dispersion covering a large energy and momentum scale along the $\overline{M}$-$\overline{\Gamma}$-$\overline{M}$ direction measured by photons with mixed polarization (inset, with both components perpendicular and parallel to the $\overline{\Gamma}$-$\overline{M}$ direction, more details can be found in Supplementary Information, part A). **b**, Band dispersion measured with photon polarization parallel to the $\overline{\Gamma}$-$\overline{M}$ direction (inset) shows the enhanced Dirac band. **c**, Fermi surface map across the whole 3D Brillouin zone (top panel) and its projection onto the surface Brillouin zone in the k_x-k_y plane (bottom panel). High-symmetry points in the Brillouin zone are marked in the plot; and the grey arrows indicate the [001] and [111] directions. **d**, Four measurements at different k_z (indicated by yellow dashed lines in **c**), showing the evolution of the band dispersion from a hyperbolic (i–iii) to a linear (iv) shape. The overlaid red dashed curves are the fitted band dispersions (see text and Supplementary Information, part C for details), showing excellent agreement with the experiments.

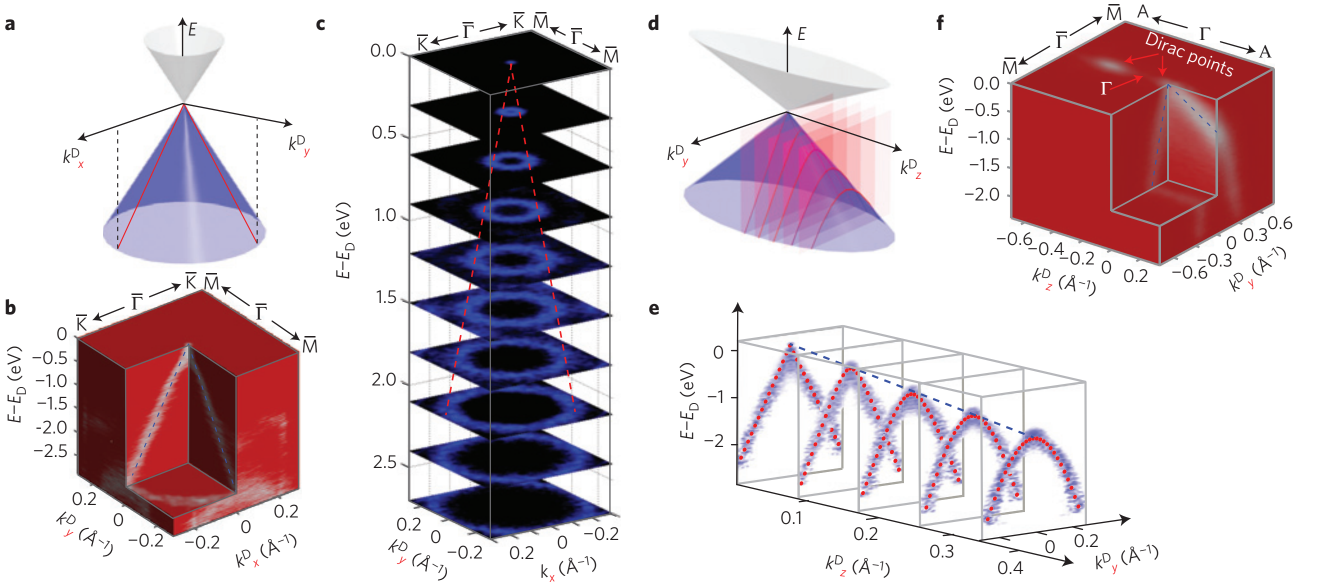

Figure 3 | Projections of the 3D Dirac fermions into (k_x, k_y, E) and (k_y, k_z, E) space. a, Schematic of projected Dirac cone into the (k_x, k_y, E) space reconstructed from the experimental parameters. Red lines indicate the linear dispersions along the k_x and k_y directions. **b**, 3D intensity plot of the photoemission spectra at the Dirac point, showing cone-shape dispersion similar to that in **a**. **c**, Stacking plots of constant-energy contours at different binding energies show Dirac cone band structure. Red dotted lines are guides to the eye that indicate the dispersions and intersect at the Dirac point. **d**, Schematic of projected Dirac cone into the (k_y, k_z, E) space reconstructed from the experimental parameters. The pink planes indicate the ARPES measurements that slice through the Dirac cone at different k_z positions, resulting in either linear or hyperbolic dispersions (red curves). **e**, Five measured dispersions at different k_z positions (as shown in **d**). Red dotted curves show fitted band dispersions that agree well with the experiments. The blue dashed line is a guide to the eye that connects the band top of each measurement, showing a linear dispersion along the k_z direction. **f**, 3D intensity plot of the photoemission spectra at the Dirac point in the (k_y, k_z, E) space, showing the elongated Dirac cone along the k_z direction.

with V_x and V_y obtained above, $V_z = 0.25V_y$, indicating a large out-of-plane anisotropy.

The details of the band dispersions along all three momentum directions can be summarized in Fig. 4a–c, where the dispersions along each k direction evolve from a linear (Fig. 4a–c(i)) to a hyperbolic (Fig. 4a–c(ii–iv)) shape as expected. Remarkably, to fit all of these dispersions, we need only one set of 3D Dirac cone parameters ($V_x = 8.47$ eV Å or 1.28×10^6 m s^{-1}, $V_y = 8.56$ eV Å

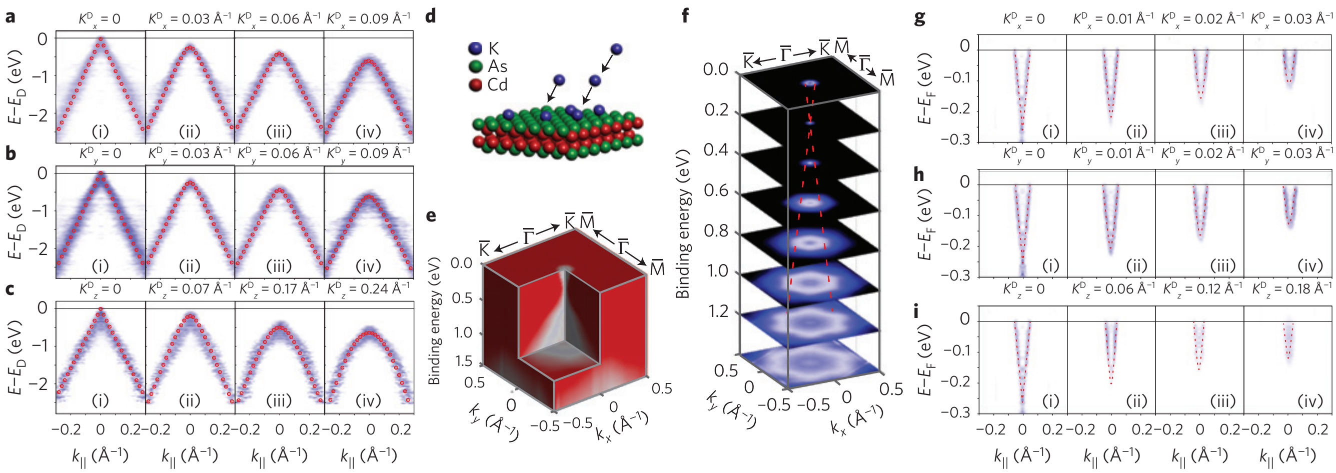

Figure 4 | Dispersion of the 3D Dirac fermion along all three momentum directions and E_F tuning by alkaline surface doping. a–c, Band dispersions measured at a series of k_x, k_y and k_z values. Red dotted curves are fitted dispersions by using only one set of velocity parameters ($V_x = 8.47$ eV Å, $V_y = 8.56$ eV Å and $V_z = 2.16$ eV Å), showing excellent agreement with all measurements. **d**, Illustration of the *in situ* electron doping using an alkaline (potassium) metal dispenser. **e**, 3D intensity plot of the photoemission spectra at the Dirac point after K surface doping, showing the upper Dirac cone. **f**, Stacking plots of constant-energy contours at different binding energies after K dosing, showing the Dirac point that connects the upper and lower cones, with $E_F \sim 250$ meV above the Dirac point. Red dashed lines are guides to the eye that trace the Dirac dispersions. **g–i**, Band dispersions of the upper Dirac cone measured after K-dosing with fitted dispersions (red dotted curves, note that the spectra plotted are the second derivatives of the photoemission intensity to improve contrast), proving the linear dispersions of the upper Dirac cone along all three momentum directions.

or 1.3×10^6 m s^{-1} and $V_z = 2.16$ eV Å or 3.27×10^5 m s^{-1}). These excellent overall agreements unambiguously prove that the bulk band structure of Cd_3As_2 forms 3D Dirac fermions.

As the E_F of the measured sample is pinned at the Dirac point, the upper Dirac cone was unoccupied, and thus cannot be seen by the ARPES measurements above. To visualize it, we introduced *in situ* electron doping using an alkaline metal doser (Fig. 4d) to raise the E_F—and successfully lifted E_F to ~250 meV above the Dirac point. The effect can be clearly seen from both the 3D ARPES spectra (Fig. 4e) and the band structure contour (Fig. 4f) plots, where the upper and lower Dirac cones touch at the Dirac point. With this achievement, we can extract the dispersions of the upper Dirac cone along all three momentum directions (Fig. 4g–i), which again clearly show linear dispersion along each momentum direction. Interestingly, we observed that the fitted velocities of the upper Dirac cone show a reduced value ($V_x = 5$ eV Å or 7.55×10^5 m s^{-1}, $V_y = 5.1$ eV Å or 7.7×10^5 m s^{-1} and $V_z = 1.5$ eV Å or 2.27×10^5 m s^{-1}) compared with that of the lower cone (that is, the valence band), in agreement with the theoretical calculation[6].

The observation of bulk Dirac fermions clearly proves that Cd_3As_2 is a model system of the 3D TDS, making it the first stable 3D counterpart of graphene—as other 3D TDS candidates proposed so far, including the A_3Bi (A = Na, K, Rb) family of compounds[4,5] and β-cristobalite BiO_2 (ref. 3), are all unstable in ambient environment. Furthermore, the unusually high Fermi velocity ($V_x/V_y/V_z$ of Cd_3As_2 are about 3.5/3.5/11 times larger than those of Na_3Bi; ref. 5) and mobility of its bulk carriers[16], as well as the tunability of E_F, also makes it a practical candidate for fabricating functional devices where precise control of the carrier density (thus, the E_F position) is necessary.

Note added in proof: Finally, we note that while we were finalizing this manuscript, two other groups also independently studied Cd_3As_2 and showed an indication of the 3D Dirac fermions in this compound[26,27].

Methods

Sample synthesis. High-quality Cd_3As_2 single crystals were synthesized by placing stoichiometric amounts of high-purity (>99.99%) Cd and As elements inside an evacuated carbon-coated quartz tube, which was sealed in another evacuated tube for extra protection. The two tubes were then placed inside a two-zone furnace and heated to 850 °C. After 6 h the furnace was cooled to 550 °C at a rate of 2.5 °C h^{-1}, and finally it was cooled down to room temperature at the rate of 60 °C h^{-1}.

Angle-resolved photoemission spectroscopy. ARPES measurements were performed at beamline 10.0.1 of the Advanced Light Source (ALS) at Lawrence Berkeley National Laboratory and beamline I05 of the Diamond Light Source (DLS). The measurement pressure was kept below $3 \times 10^{-11}/8 \times 10^{-11}$ Torr in ALS/DLS, and data were recorded by Scienta R4000 analysers at 10/80 K sample temperature at ALS/DLS. The total convolved energy and angle resolutions were 16 meV/30 meV and 0.2°/0.2° at ALS/DLS, respectively. The fresh surface for ARPES measurement was obtained by cleaving the Cd_3As_2 sample *in situ* along its natural cleavage plane.

***In situ* electron doping.** The *in situ* electron doping was realized by evaporating potassium onto the sample surface in the ultrahigh-vacuum measurement chamber. The experiment was done at ALS under a vacuum better than 5×10^{-11} Torr.

Local-density approximation calculations. The electronic band calculations were performed within the density functional formalism as implemented in the Vienna *ab initio* simulation package[28,29]. We use the all-electron projector augmented wave basis sets with the generalized gradient approximation of Perdew, Burke and Ernzerhof[29,30] to the exchange correlation potential. The spin–orbit coupling was taken into account self-consistently. As ARPES measurements show an averaged effect of Cd vacancies indicated by the hexagonal Brillouin zone on the (111) surface, we took the random effect of Cd vacancies by starting from a hypothetical zinc-blende structure with a simplest unit of fcc cell (different from the previous work[5]). The low-energy band structure was then captured by constructing maximally localized Wannier functions of Cd *s*- and As *p*-orbitals. The band inversion due to Cd vacancy[5] is obtained by adjusting the on-site energy of Cd *s*- and As p_z-orbitals to match the ARPES measurements.

Received 12 December 2013; accepted 24 April 2013; published online 25 May 2014

References

1. Wan, X., Turner, A. M., Vishwanath, A. & Savrasov, S. Y. Topological semimetal and Fermi-arc surface states in the electronic structure of pyrochlore iridates. *Phys. Rev. B* **83,** 205101 (2011).
2. Burkov, A. A. & Balents, L. Weyl semimetal in a topological insulator multilayer. *Phys. Rev. Lett.* **107,** 127205 (2011).

3. Young, S. M. *et al.* Dirac semimetal in three dimensions. *Phys. Rev. Lett.* **108,** 140405 (2012).
4. Wang, Z. *et al.* Dirac semimetal and topological phase transitions in A_3Bi (A = Na, K, Rb). *Phys. Rev. B* **85,** 195320 (2012).
5. Liu, Z. K. *et al.* Discovery of a three-dimensional topological Dirac semimetal, Na_3Bi. *Science* **343,** 864–867 (2014).
6. Wang, Z., Weng, H., Wu, Q., Dai, X. & Fang, Z. Three-dimensional Dirac semimetal and quantum transport in Cd_3As_2. *Phys. Rev. B* **88,** 125427 (2013).
7. Xu, G., Weng, H., Wang, Z., Dai, X. & Fang, Z. Chern semimetal and the quantized anomalous Hall effect in $HgCr_2Se_4$. *Phys. Rev. Lett.* **107,** 186806 (2011).
8. Qi, X-L. & Zhang, S-C. Topological insulators and superconductors. *Rev. Mod. Phys.* **83,** 1057–1110 (2011).
9. Fu, L. & Kane, C. L. Superconducting proximity effect and Majorana fermions at the surface of a topological insulator. *Phys. Rev. Lett.* **100,** 096407 (2008).
10. Hasan, M. Z. & Kane, C. L. Colloquium: Topological insulators. *Rev. Mod. Phys.* **82,** 3045–3067 (2010).
11. Herring, C. Accidental degeneracy in the energy bands of crystals. *Phys. Rev.* **52,** 365–373 (1937).
12. Shuichi, M. Phase transition between the quantum spin Hall and insulator phases in 3D: Emergence of a topological gapless phase. *New J. Phys.* **9,** 356 (2007).
13. Volovik, G. E. in *Quantum Analogues: From Phase Transitions to Black Holes and Cosmology* (eds Unruh, W. G. & Schützhold, R.) Ch. 3, 31–73 (Lecture Notes in Physics, Vol. 718, Springer, 2007).
14. Geim, A. K. & Novoselov, K. S. The rise of graphene. *Nature Mater.* **6,** 183–191 (2007).
15. Castro Neto, A. H., Guinea, F., Peres, N. M. R., Novoselov, K. S. & Geim, A. K. The electronic properties of graphene. *Rev. Mod. Phys.* **81,** 109–162 (2009).
16. Zdanowicz, W. & Zdanowicz, L. Semiconducting compounds of the AII BV group. *Annu. Rev. Mater. Sci.* **5,** 301–328 (1975).
17. Abrikosov, A. A. Quantum magnetoresistance. *Phys. Rev. B* **58,** 2788–2794 (1998.).
18. Zhang, W. *et al.* Topological aspect and quantum magnetoresistance of β-Ag_2Te. *Phys. Rev. Lett.* **106,** 156808 (2011).
19. Liu, C-X. *et al.* Oscillatory crossover from two-dimensional to three-dimensional topological insulators. *Phys. Rev. B* **81,** 041307 (2010).
20. Röber, E., Hackstein, K., Coufal, H. & Sotier, S. Magnetic susceptibility of liquid $Na_{1-x}Bi_x$ alloys. *Phys. Status Solidi B* **93,** K99–K102 (1979).
21. Koshino, M. & Ando, T. Anomalous orbital magnetism in Dirac-electron systems: Role of pseudospin paramagnetism. *Phys. Rev. B* **81,** 195431 (2010).
22. Kane, C. L. & Mele, E. J. Quantum spin Hall effect in graphene. *Phys. Rev. Lett.* **95,** 226801 (2005).
23. Steigmann, G. A. & Goodyear, J. The crystal structure of Cd_3As_2. *Acta Crystallogr. B* **24,** 1062–1067 (1968).
24. Damascelli, A., Hussain, Z. & Shen, Z-X. Angle-resolved photoemission studies of the cuprate superconductors. *Rev. Mod. Phys.* **75,** 473–541 (2003).
25. Chen, Y. Studies on the electronic structures of three-dimensional topological insulators by angle resolved photoemission spectroscopy. *Front. Phys.* **7,** 175–192 (2012).
26. Borisenko, S. *et al.* Experimental realization of a three-dimensional Dirac semimetal. Preprint at http://arXiv.org/abs/1309.7978 (2013).
27. Neupane, M. *et al.* Observation of a three-dimensional topological Dirac semimetal phase in high-mobility Cd_3As_2. *Nature Commun.* **5,** 3786 (2014).
28. Kresse, G. & Furthmüller, J. Efficient iterative schemes for ab initio total-energy calculations using a plane-wave basis set. *Phys. Rev. B* **54,** 11169–11186 (1996).
29. Perdew, J. P., Burke, K. & Ernzerhof, M. Generalized gradient approximation made simple. *Phys. Rev. Lett.* **77,** 3865–3868 (1996).
30. Koelling, D. D. & Harmon, B. N. A technique for relativistic spin-polarised calculations. *J. Phys. C* **10,** 3107–3114 (1977).

Acknowledgements

Y.L.C. and B.Z. acknowledge the support from the EPSRC (UK) grant EP/K04074X/1 and a DARPA (US) MESO project (no. N66001-11-1-4105). Z.K.L. and Z.X.S. acknowledge support from the Department of Energy, Office of Basic Energy Science (contract DE-AC02-76SF00515). The Advanced Light Source is operated by the Department of Energy, Office of Basic Energy Science (contract DE-AC02-05CH11231). Z.F., X.D. and H.M.W. acknowledge the support by the NSF of China, the National Basic Research Program of China, and the International Science and Technology Cooperation Program of China. J.J. and D.L.F. acknowledge the support by the NSF of China, the National Basic Research Program of China under grant no. 2012CB921402. J.J. acknowledges the support from the China Scholarship Council.

Author contributions

Y.L.C. conceived the experiments. Y.L.C., Z.K.L., J.J. and B.Z. carried out ARPES measurements with the assistance of P.D., T.K., M.H. and S-K.M. D.P. synthesized and characterized bulk single crystals. Z.J.W. and H.M.W. performed *ab initio* calculations. All authors contributed to the scientific planning and discussions.

Additional information

Supplementary information is available in the online version of the paper. Reprints and permissions information is available online at www.nature.com/reprints. Correspondence and requests for materials should be addressed to Y.L.C.

Competing financial interests

The authors declare no competing financial interests.